

# THE HAWAII SCUBA-2 LENSING CLUSTER SURVEY: ARE LOW-LUMINOSITY SUBMILLIMETER GALAXIES DETECTED IN THE REST-FRAME UV?

LI-YEN HSU (徐立研)<sup>1</sup>, LENNOX L. COWIE<sup>1</sup>, AMY J. BARGER<sup>1,2,3</sup>, AND WEI-HAO WANG (王為豪)<sup>4</sup>

*Draft version December 14, 2024*

## ABSTRACT

In this third paper of the Hawaii SCUBA-2 Lensing Cluster Survey series, we present Submillimeter Array (SMA) detections of six intrinsically faint 850  $\mu\text{m}$  sources detected in SCUBA-2 images of the lensing cluster fields, A1689, A2390, A370, MACS J0717.5+3745, and MACS J1423.8+2404. Two of the SCUBA-2 sources split into doublets, yielding a total of eight SMA detections. The intrinsic 870  $\mu\text{m}$  flux densities of these submillimeter galaxies (SMGs) are  $\sim 1$  mJy. Five of the eight SMGs are not detected in optical or near-infrared (NIR) images. The NIR-to-submillimeter flux ratios of these faint SMGs suggest that most of them are extremely dusty and/or at very high redshifts. Combining these SMGs and several other samples from the literature, we find a bimodal distribution for the faint sources in the space of submillimeter flux versus NIR-to-submillimeter flux ratio. While most of the SMA-detected lensed sources are very obscured, the other SMGs with similar flux densities are mostly bright in the NIR. Future ALMA observations of a large sample of SCUBA-2 sources in cluster fields will allow us to decide whether the bimodality we observe here really exists.

*Subject headings:* cosmology: observations— galaxies: formation — galaxies: starburst — gravitational lensing: strong — submillimeter: galaxies

## 1. INTRODUCTION

The measurements of the far-infrared (FIR) Extragalactic Background Light (EBL) demonstrated that about half of the starlight in the optical and ultraviolet (UV) is absorbed by dust and re-radiated into the FIR (Puget et al. 1996; Fixsen et al. 1998; Dole et al. 2006). It is therefore important to study both the unobscured and dust-obscured populations of galaxies across cosmic time for a full picture of star formation in our universe. At high redshifts, observations at submillimeter/millimeter wavelengths provide insight on such dusty star formation. However, submillimeter surveys with even 15 m telescopes such as the James Clerk Maxwell Telescope (JCMT) become confusion limited (Condon 1974) at  $\lesssim 2$  mJy at 850  $\mu\text{m}$ , which prevents the detection of fainter submillimeter galaxies (SMGs; see reviews by Blain et al. 2002; Casey et al. 2014) with infrared luminosities  $\lesssim 10^{12} L_{\odot}$ .

Bright SMGs from confusion-limited surveys and the extinction-corrected UV population are essentially disjoint (e.g., Barger et al. 2014; Cowie et al. 2017), so their contributions to the cosmic star formation history (Madau & Dickinson 2014) must be added. Fainter SMGs, on the other hand, are more common objects that contribute the majority of the EBL (e.g., Chen et al. 2013; Hsu et al. 2016; Zavala et al. 2017) and therefore most of the dusty star formation. However, some of these faint SMGs could also be selected in the UV samples. In order to combine the UV- and FIR-inferred star formation history precisely, it is critical to obtain a complete census of faint SMGs that have star formation rates (SFRs) comparable to those of the UV population. Such a sample bridges the SFR gap between the two populations and

allows us to determine if there is a critical SFR below which UV-selected galaxies alone account for all the star formation.

Imaging of massive galaxy cluster fields is a good way to detect intrinsically fainter sources, thanks to gravitational lensing. Lensed sources are magnified at all wavelengths, and their images benefit from enhanced spatial resolution. Direct searches for SMGs using interferometry are very inefficient due to the small field of views. Thus, deep and wide-field surveys with single-dish submillimeter/millimeter telescopes are the most efficient approach to search for SMGs (at least down to their confusion limits).

The SCUBA-2 camera (Holland et al. 2013) on the JCMT is currently the most powerful instrument for submillimeter surveys. Among all the ground-based submillimeter instruments, SCUBA-2 has the best angular resolution ( $\sim 14''$  at 850  $\mu\text{m}$  and  $7''$  at 450  $\mu\text{m}$ ), yielding more accurate positions, less source blending, and a lower confusion limit. We have been undertaking a SCUBA-2 program, the Hawaii SCUBA-2 Lensing Cluster Survey (Hawaii-S2LCS), to image nine massive clusters. These include the northern five clusters in the *HST* Frontier Fields program (Lotz et al. 2017). We have presented deep number counts at 450 and 850  $\mu\text{m}$  in Hsu et al. (2016) and a radio-detected sample of faint SMGs in Hsu et al. (2017).

Due to the low spatial resolution of single-dish telescopes, interferometric follow-up is required to identify the multi-wavelength counterparts to submillimeter sources. Thus, we have also been using the Submillimeter Array (SMA; Ho et al. 2004) to image some of our SCUBA-2 sources. In this third paper of the Hawaii-S2LCS series, we present our SMA follow-up observations of six intrinsically faint SCUBA-2 sources discovered in the fields of A1689, A2390, A370, MACS J0717.5+3745, and MACS J1423.8+2404 (hereafter, MACSJ0717 and MACSJ1423). The observations and data reduction are described in Section 2. We present our results in Section 3 and discuss their implications in Section 4. Section 5 summarizes this paper. We assume the concordance  $\Lambda$ CDM cosmology with  $H_0 = 70 \text{ km s}^{-1} \text{ Mpc}^{-1}$ ,

<sup>1</sup> Institute of Astronomy, University of Hawaii, 2680 Woodlawn Drive, Honolulu, HI 96822, USA

<sup>2</sup> Department of Astronomy, University of Wisconsin-Madison, 475 North Charter Street, Madison, WI 53706, USA

<sup>3</sup> Department of Physics and Astronomy, University of Hawaii, 2505 Correa Road, Honolulu, HI 96822, USA

<sup>4</sup> Academia Sinica Institute of Astronomy and Astrophysics, P.O. Box 23-141, Taipei 10617, Taiwan

$\Omega_M = 0.3$ , and  $\Omega_\Lambda = 0.7$ . All magnitudes used are AB magnitudes.

## 2. DATA

### 2.1. SCUBA-2 Observations

The targets for the SMA observations were selected from our SCUBA-2 lensing cluster surveys, based on the 850  $\mu\text{m}$  images we had at different times. However, the SCUBA-2 measurements we present in this work (Section 3) are based on all the 850  $\mu\text{m}$  data taken with the CV DAISY scan pattern between February 2012 and March 2017. We summarize these observations in Table 1. Please refer to Hsu et al. (2016) and Hsu et al. (2017) for details on the data reduction and source extraction procedures. In order to correct for the effects of Eddington bias (Eddington 1913) and confusion noise (Condon 1974), we deboosted the SCUBA-2 flux densities based on their signal-to-noise ratios (S/N) using the Monte Carlo simulations described in Hsu et al. (2017).

### 2.2. SMA Observations

We carried out SMA observations from 2014 to 2016 of six SCUBA-2 850  $\mu\text{m}$  sources in the five cluster fields. The local oscillator frequency was set at 343 GHz, or 870  $\mu\text{m}$ . The new SWARM (SMA Wideband Astronomical ROACH2 Machine) correlator and dual receiver mode became available during the course of our program, which greatly improved the continuum sensitivity. We summarize these observations in Table 2.

We used the SMA data reduction package MIR to calibrate our data. The visibilities were first weighted in inverse proportion to the square of the system temperatures. The continuum data were generated by averaging all the spectral channels after performing passband phase calibration. We used the gain calibrators to correct for the variations of phase/amplitude in time, and then we performed the flux calibration to set the absolute flux level. For the track executed in dual receiver mode (20161017 in Table 2), we ran all the calibrations for the two receivers separately.

The visibilities from all the available tracks for each source were combined and imaged using the interferometry data reduction package MIRIAD (Sault et al. 1995). We made the dirty maps and the synthesized dirty beam images in a  $0''.2$  (compact configuration) or  $0''.1$  (extended configuration) grid using the routine INVERT with natural weighting on the baselines. We also performed multi-frequency synthesis, which gives better coverage in the frequency-dependent uv coordinate. The CLEAN routine was used to deconvolve the dirty map. We CLEANed the images around detected sources to approximately  $1.5\sigma$  to remove the effects of sidelobes. The resulting source fluxes are not sensitive to the depth to which we chose to clean. Primary beam correction was applied to the images by dividing the CLEANed fluxes by the off-axis gain. In Table 3, we summarize the synthesized beams and central sensitivities of the final images.

### 2.3. HST and Spitzer Images

For the Frontier Field clusters, we retrieved the Advanced Camera for Surveys (ACS) and Wide-Field Camera 3 (WFC3) images from the HST Frontier Field archive<sup>5</sup>. The images for MACSJ1423 are taken from the Cluster Lensing And Supernova survey with Hubble (CLASH; Postman et al. 2012)

archive<sup>6</sup>. For A1689 and A2390, we used SWARP (Bertin et al. 2002) to combine individual archival images<sup>7</sup> for each passband. We also retrieved the Spitzer Frontier Fields data<sup>8</sup>, as well as the ‘‘Super Mosaics’’ and their source catalogs for the other three clusters from the Spitzer archive.

### 2.4. $K_s$ -band Images

We carried out  $K_s$ -band observations of A1689 and A2390 (PI: Hsu; PID: 15AH83) with WIRCam on the Canada–France–Hawaii Telescope (CFHT) in 2015. Along with the archival data of A2390 (PI: Umetsu; PID: 07AT98), the total integration times are 2800 and 3515 seconds for A1689 and A2390, respectively. We reduced and combined these images using Imaging and Mosaicking PipeLinE (SIMPLE; Wang et al. 2010), an IDL-based package for galactic/extragalactic imaging with CFHT/WIRCam.

SIMPLE performs flat fielding, background subtraction, distortion correction, absolute astrometry, photometric calibration, wide-field mosaicking, cosmic ray removal, and image weighting. Absolute astrometry was obtained by comparing the image with the source catalogs of the Sloan Digital Sky Survey (SDSS). The photometry was calibrated with bright stars in the source catalogs of the Two Micron All Sky Survey (2MASS). We reduced the data chip by chip before mosaicking, and the pixel scale of the images is  $0''.3$ . The images reach  $3\sigma$  limiting magnitudes of 23.8 and 24.0 in a  $1''$ -radius aperture for A1689 and A2390, respectively.

We also retrieved the  $K_s$ -band images of the Frontier Fields A370 (VLT/HAWK-I), MACSJ0717 (Keck/MOSFIRE), and MACSJ1423 (CFHT/WIRCam) from Brammer et al. (2016) and the CLASH archive, respectively.

### 2.5. VLA Images

We make use of the 3 GHz image of MACSJ0717 taken with the Karl G. Jansky Very Large Array (VLA) from Hsu et al. (2017), which has a synthesized beam of  $\sim 0''.4$  and a sensitivity of  $\sim 1\ \mu\text{Jy}$ . For A370 and A2390, we obtained the VLA 1.4 GHz images from Wold et al. (2012). The A370 (A2390) image has a synthesized beam of  $\sim 1''.7$  ( $1''.4$ ) and a noise level of  $\sim 5.7$  ( $5.6$ )  $\mu\text{Jy}$  near the cluster center.

## 3. RESULTS

### 3.1. SMA Detections and Multiwavelength Counterparts

We detected eight sources above a  $4\sigma$  level in the six SMA images, where SMA-2 and SMA-3 both split into doublets. The positions and flux densities of the original SCUBA-2 sources and these SMA detections are summarized in Table 4. In Figure 1, we show the postage stamp images centered at the original SCUBA-2 positions. Although there is more than a factor of 2 discrepancy between the SCUBA-2 and SMA flux densities for SMA-1 and SMA-6, the difference can be caused by multiple faint sources that are below our detection limit. This is clear for SMA-6, where we can see some emission with  $S/N > 3$  coming from an optically detected galaxy (possibly a pair of interacting galaxies).

Three (SMA-1, SMA-2-1, and SMA-5) of the eight SMA sources are detected in the optical or NIR. Note that for SMA-4, there is one elliptical galaxy that has a  $< 1''$  offset from

<sup>6</sup> <https://archive.stsci.edu/prepds/clash/>

<sup>7</sup> PI (PIDs): Blakeslee (11710), Ellis (10504), Ford (9289, 11802), Rigby (11678), Siana (12201, 12931)

<sup>8</sup> <http://irsa.ipac.caltech.edu/data/SPITZER/Frontier/>

<sup>5</sup> <https://archive.stsci.edu/pub/hlsp/frontier/>

TABLE 1  
SUMMARY OF JCMT/SCUBA-2 OBSERVATIONS

Field	R.A.	Decl.	Redshift	Weather <sup>a</sup>	Exposure <sup>b</sup> (hr)	$\sigma_{850}^c$ (mJy beam <sup>-1</sup> )
A370	02 39 53.1	-01 34 35.0	0.375	1+2+3	28.5+1.5+7.0	0.38
MACSJ0717	07 17 34.0	37 44 49.0	0.545	1+2+3	32.2+10.5+1.5	0.31
A1689	13 11 29.0	-01 20 17.0	0.184	1+2	22.4+1.9	0.39
MACSJ1423	14 23 48.3	24 04 47.0	0.545	1+2+3	36.5+20.5+1.6	0.28
A2390	21 53 36.8	17 41 44.2	0.231	1+2+3	17.4+36.0+9.0	0.32

<sup>a</sup>Data were taken in band 1 ( $\tau_{225\text{GHz}} < 0.05$ ), band 2 ( $0.05 < \tau_{225\text{GHz}} < 0.08$ ), or good band 3 ( $0.08 < \tau_{225\text{GHz}} < 0.1$ ) conditions.

<sup>b</sup>Integration times of the three weather conditions.

<sup>c</sup>Central  $1\sigma$  sensitivity of the 850  $\mu\text{m}$  map. These are the statistical/instrumental noise values directly from the reduced rms maps.

TABLE 2  
SUMMARY OF SMA OBSERVATIONS

ID	Field	Configuration	Track Dates	Receiver(s)	Bandwidth <sup>a</sup>	Passband Calibrator	Gain Calibrator(s)	Flux Calibrator(s)
SMA-1	A370	extended	20151001	345	8 GHz	3c454.3	0224+069, 0309+104	Neptune
			20161017	345, 400 <sup>b</sup>	12 GHz	3c454.3	0224+069, 0309+104	Uranus
SMA-2	MACSJ0717	compact	20160102	345	8 GHz	3c84	0818+423, 0927+390	Neptune
SMA-3	A1689		20160104	345	12 GHz	3c279	1337-129, 3c279	Callisto
SMA-4	MACSJ1423	compact	20160301	345	8 GHz	3c273	1504+104	Ganymede
			20160308	345	8 GHz	3c273	1357+193, 1415+133	Ganymede
SMA-5	A2390	compact	20140625	345	8 GHz	3c279	2148+069, 3c454.3	Titan, Neptune
			20140626	345	8 GHz	3c279	2148+069, 3c454.3	Neptune
			20141024	345	8 GHz	3c454.3	2148+069, 3c454.3	Neptune
			20141029	345	8 GHz	3c454.3	2148+069, 3c454.3	Neptune
			20141030	345	8 GHz	3c454.3	2148+069, 3c454.3	Neptune
SMA-6	A2390	compact	20140629	345	8 GHz	3c279	2148+069, 3c454.3	Titan, Neptune
			20140630	345	8 GHz	3c279	2148+069, 3c454.3	Titan, Neptune
			20140702	345	8 GHz	3c454.3	2148+069, 3c454.3	Titan, Neptune
			20141024	345	8 GHz	3c454.3	2148+069, 3c454.3	Neptune
			20141029	345	8 GHz	3c454.3	2148+069, 3c454.3	Neptune

<sup>a</sup>Total bandwidth combing upper and lower sidebands. When the SWARM correlator operated, an additional 2 GHz was available for each sideband.

<sup>b</sup>Dual receiver mode. The two receivers cover the same spectral range.

TABLE 3  
SYNTHESIZED BEAM SIZES AND POSITION ANGLES AS WELL AS  
CENTRAL SENSITIVITIES OF THE SMA IMAGES

ID	Beam FWHM (" × ")	Beam P.A. (deg)	$\sigma$ (mJy beam <sup>-1</sup> )
SMA-1	0.86 × 0.60	85.0	0.44
SMA-2	2.20 × 1.88	-64.6	0.38
SMA-3	2.03 × 1.92	-0.9	0.50
SMA-4	2.15 × 1.78	-86.3	0.48
SMA-5	2.28 × 1.60	-73.9	0.55
SMA-6	2.21 × 1.53	-83.0	0.43

the SMA position. Based on the photometric catalog from CLASH, this source is a cluster member galaxy at  $z \sim 0.5$ . Thus, it is unlikely to be the counterpart to the SMG. There is also a small offset between the peaks of the submillimeter and optical emission for SMA-5. However, the offset becomes smaller in the  $K_s$ -band image. We suggest that the optical/NIR source is the correct counterpart to the SMG, and the offset is due to different regions of unobscured and dust-obscured star formation, which is very typical for SMGs.

As we will discuss in Section 4, we use  $K_s$ -band photometry to quantify the NIR emission, given that  $K_s$ -band images

are available for all of our sources. In addition, they have better spatial resolution than the *Spitzer* images. We used SExtractor (Bertin & Arnouts 1996) to measure AUTO magnitudes of the SMA sources detected at  $K_s$  band. The deblending parameters DEBLEND\_NTHRESH and DEBLEND\_MINCONT were set to be 32 and 0.005, respectively. For the sources that are not detected in the  $K_s$ -band images, we measured their  $3\sigma$  limiting magnitudes in a  $1''$ -radius aperture.

### 3.2. Redshift Estimates

We measured the photometric redshifts of SMA-1 and SMA-5 using the BPZ code (Bayesian photometric redshift estimation; Benítez 2000) and the Bruzual & Charlot (2003) models with the Chabrier (2003) initial mass function. SMA-1 is covered by *HST* observations at F435W, F606W, F814W, F110W, F140W, and F160W. We ran SExtractor in dual-image mode using F160W as the detection band to obtain AUTO magnitudes. The deblending parameters DEBLEND\_NTHRESH and DEBLEND\_MINCONT were again chosen to be 32 and 0.005, respectively. For SMA-5, F850LP is the only available *HST* passband. We took the IRAC  $1.9''$ -radius aperture photometry from the *Spitzer* source catalog of A2390 and ran SExtractor in single-image mode to measure the AUTO magnitudes at F850LP and  $K_s$ . Before running BPZ, we corrected all the magnitudes for Galactic dust

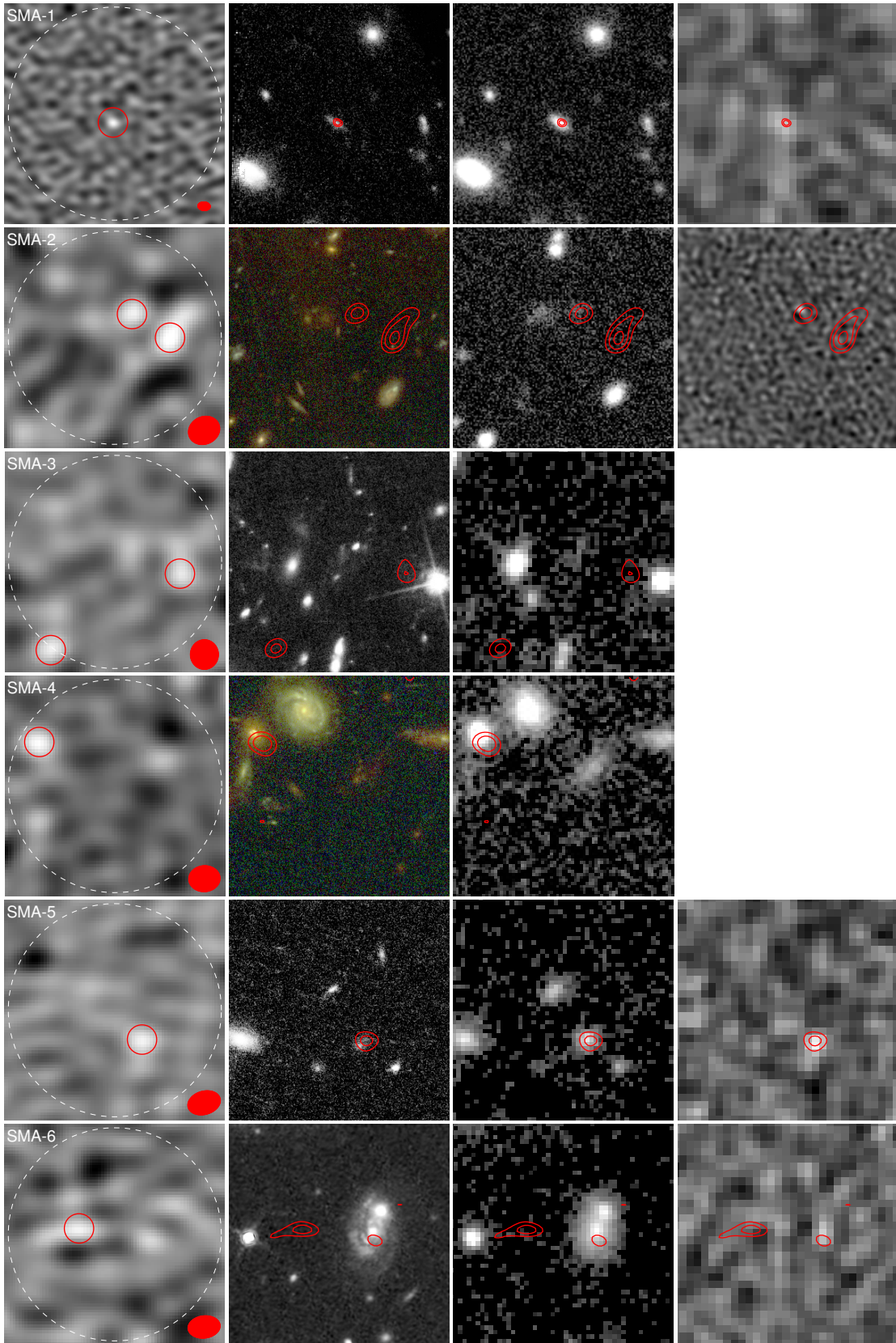


FIG. 1.— Postage stamp images for the SMA detections centered at the SCUBA-2 850  $\mu\text{m}$  positions. From left to right are SMA 870  $\mu\text{m}$ , *HST* (from top to bottom: F160W, F435W-F606W-F814W false color, F814W, F435W-F606W-F814W false color, F850LP, and F125W),  $K_s$ -band (SMA-1: VLT/HAWK-I, SMA-2: Keck/MOSFIRE; SMA-3, SMA-4, SMA-5, and SMA-6: CFHT/WIRCam), and VLA (SMA-1, SMA-5, and SMA-6: 1.4 GHz; SMA-2: 3 GHz) images. The image size is  $15'' \times 15''$ . In the SMA images, the large dashed circles with a diameter of  $14''/5$  represent the JCMT beam (FWHM); we use  $1''$ -radius red circles to denote the SMA detections, and the ellipses at the bottom-right corners represent the synthesized beams. The red contours in the other images are  $(3, 4, 5) \times \sigma$  isophotes of the SMA sources.

extinction from Schlafly & Finkbeiner (2011). We obtained  $z = 2.39 \pm 0.17$  and  $2.00 \pm 0.15$  for SMA-1 and SMA-5, respectively.

For SMA-2-1, SMA-2-2 and SMA-6, we used the submillimeter-to-radio flux ratios to compute their “millimetric redshifts”, following the method in Barger et al. (2000). The relation between the redshift and the submillimeter-to-radio flux ratio is

$$\begin{aligned} z &= (S_{343\text{GHz}}/S_{1.4\text{GHz}})^{0.26} - 1 \\ &= 0.85(S_{343\text{GHz}}/S_{3\text{GHz}})^{0.26} - 1 \end{aligned} \quad (1)$$

With  $S_{3\text{GHz}} = 5.13 \pm 1.51 \mu\text{Jy}$  (Hsu et al. 2017), we obtained  $z = 2.9 \pm 0.4$  for SMA-2-1. Because SMA-2-2 and SMA-6 are not detected in the radio images, we used their  $3\sigma$  limits,  $3.05 \mu\text{Jy}$  (3 GHz) and  $22.6 \mu\text{Jy}$  (1.4 GHz), to compute the lower redshift limits. The results are  $z > 3.7$  and  $z > 2.2$  for SMA-2-2 and SMA-6, respectively. Note that SMA-1 and SMA-5 are also detected at 1.4 GHz with  $S_{1.4\text{GHz}} = 26.9 \pm 6.2 \mu\text{Jy}$  and  $35.8 \pm 6.9 \mu\text{Jy}$ , respectively. Their millimetric redshifts are  $2.1 \pm 0.3$  and  $2.0 \pm 0.2$ , respectively, in agreement with the photometric redshifts.

For the three SMA sources in A1689 and MACSJ1423, there are no deep radio images available. Because these sources are not detected in *HST*,  $K_s$ -band, or *Spitzer* images, we expect them to be at high redshifts. We assume a conservative lower limit at  $z = 1.0$  to estimate their lensing magnifications, which we will describe in the next section.

### 3.3. Lens Models

In order to compute the magnifications and intrinsic flux densities of our faint SMGs, the lens models of the clusters and source redshifts are required. A set of lens models are available for the *HST* Frontier Fields from ten teams, including Bradac (Bradač et al. 2005, 2009; Hoag et al. 2016), Caminha (Caminha et al. 2017), CATS (Jullo & Kneib 2009; Jauzac et al. 2012, 2014, 2015a,b; Richard et al. 2014), Diego (Diego et al. 2005a,b, 2007, 2015), GLAFIC (Oguri 2010; Kawamata et al. 2016), Keeton (Keeton 2010; Ammons et al. 2014; McCully et al. 2014), Merten (Merten et al. 2009, 2011), Sharon (Jullo et al. 2007; Johnson et al. 2014), Williams (Liesenborgs et al. 2006; Mohammed et al. 2014; Grillo et al. 2015; Sebesta et al. 2016), and Zitrin (Zitrin et al. 2009, 2013).

For A1689, A2390, and MACSJ1423, we used the models from Limousin et al. (2007), Richard et al. (2010), and the CLASH archive, respectively. Both the Frontier Fields and CLASH archives provide a set of images to account for the full range (i.e., the uncertainty) of each model, and we used the newest model from each team. On the other hand, only the best-fit models<sup>9</sup> are available for A1689 and A2390 by running the LENSTOOL software (Kneib et al. 1996). In Table 5, we tabulate the models we used for each cluster field.

Following Coe et al. (2015), we estimated the median and 68.3% range of the magnification values from Monte Carlo simulations. For each source, we propagated the positional and redshift uncertainties, as well as the full range (except for A1689 and A2390) of all the available lens models. The positional uncertainties were measured using the MIRIAD IMFIT routine, and the typical values are  $0''.1 \sim 0''.3$  in both right ascension and declination. To propagate the redshift uncertainties of SMA-2-1, SMA-2-2, SMA-3-1, SMA-3-2, SMA-

4, and SMA-6, we used a uniform distribution between their lower limits and an upper limit at  $z = 6$ . The resulting magnification error for SMA-4 is very large, because the critical lines at  $z = 1 - 6$  are close to this source. We therefore decided to only use  $z > 1.0$  to compute the lower limit of its magnification. In Table 6, we summarize the redshifts, lensing magnifications, de-lensed submillimeter flux densities, and observed  $K_s$ -band magnitudes of the SMA sources.

## 4. DISCUSSION

Five of our eight SMA sources are not detected in either the optical or NIR images. This agrees with Chen et al. (2014) and suggests that many faint SMGs are still missed by optical surveys and would not be included in the UV star formation history. However, studies of low-redshift starburst galaxies (e.g., Chary & Elbaz 2001; Le Floc’h et al. 2005; Reddy et al. 2010) have shown that fainter sources are generally less dusty. In addition, some recent work suggests that fainter SMGs are on average at lower redshifts (e.g., Heavens et al. 2004; Bundy et al. 2006; Franceschini et al. 2006; Dye et al. 2008; Mobasher et al. 2009; Magliocchetti et al. 2011; Hsu et al. 2016; Cowie et al. 2017). Based on these results, the NIR-to-submillimeter flux ratios of SMGs are expected to increase with decreasing luminosity/flux.

Recently, we have obtained different samples of SCUBA/SCUBA-2 sources followed up by the SMA (Chen et al. 2014; Cowie et al. 2017), ALMA (Cowie et al., in preparation), or VLA (Cowie et al. 2017; Hsu et al. 2017). Since  $K_s$ -band imaging is available for these samples and this work, we can combine them and inspect the change of  $K_s$ -to-submillimeter flux ratio over a wide flux range. In Figure 2 (3), we show  $K_s$ -to-870 (850)  $\mu\text{m}$  flux ratio as a function of 870 (850)  $\mu\text{m}$  flux density for the submillimeter (radio) identified samples. The 1.1 mm lensed sources in the Frontier Fields from González-López et al. (2017) and the 1.3 mm sources in the Hubble Ultra Deep Field (HUDF; Beckwith et al. 2006) from Dunlop et al. (2017)<sup>10</sup> are also included in Figure 2. We scaled their flux densities to 870  $\mu\text{m}$  values using an Arp 220 spectral energy distribution (SED; Silva et al. 1998) redshifted to their redshifts (Laporte et al. 2017; Dunlop et al. 2017). For example, the conversions are  $S_{870\mu\text{m}}/S_{1.1\text{mm}} = 1.92$  and  $S_{870\mu\text{m}}/S_{1.3\text{mm}} = 3.10$  for a source at  $z = 2$ . For the  $K_s$ -band photometry<sup>11</sup>, we ran SExtractor on the images from Brammer et al. (2016) and Fontana et al. (2014) for the 1.1 and 1.3 mm sources, respectively.

We can see in Figures 2 and 3 that most of the SMGs show a trend of increasing  $K_s$ -to-submillimeter flux ratios as we go from brighter to fainter sources. The 3 GHz-identified lensed SMGs from Hsu et al. (2017) and the faintest sources in the CDF-S ALMA sample (Cowie et al., in preparation) occupy

<sup>10</sup> The final sample of Dunlop et al. (2017) consists of sixteen  $3.5\sigma$ -detected sources that have NIR counterparts in the *HST* image. This is a clean but biased sample, since any real source without a NIR counterpart is rejected. We therefore only include their five  $6\sigma$ -detected sources, which comprise a clean and unbiased sample without the need of detections in the NIR.

<sup>11</sup> Two of the twelve 1.1 mm sources from González-López et al. (2017), A2744-ID02 and A2744-ID03, are seriously blended in the  $K_s$ -band image, so we did not measure their photometry. These two sources are therefore not included in Figures 2 and 4. Laporte et al. (2017) simply used a  $0''.4$ -radius aperture with the IRAF NOAO daophot package and applied aperture corrections to measure the magnitudes for 11 of these sources. However, here we performed our own measurements with SExtractor instead of taking their results.

<sup>9</sup> <https://projets.lam.fr/projects/lenstool/wiki>

TABLE 4  
POSITIONS AND FLUX DENSITIES OF THE SCUBA-2 SOURCES AND THEIR SMA DETECTIONS

ID	SCUBA-2			SMA		
	R.A.	Decl.	$S_{850}$ (mJy)	R.A.	Decl.	$S_{870}$ (mJy)
SMA-1	02 39 57.57	-01 34 53.0	$4.71 \pm 0.73$	02 39 57.58	-01 34 53.6	$2.14 \pm 0.44$
SMA-2	07 17 38.22	37 46 15.0	$2.97 \pm 0.63$	...	...	...
SMA-2-1	...	...	...	07 17 38.12	37 46 16.6	$1.78 \pm 0.39$
SMA-2-2	...	...	...	07 17 37.90	37 46 15.0	$2.15 \pm 0.40$
SMA-3	13 11 23.93	-01 20 46.4	$4.26 \pm 0.77$	...	...	...
SMA-3-1	...	...	...	13 11 23.64	-01 20 47.2	$2.14 \pm 0.53$
SMA-3-2	...	...	...	13 11 24.22	-01 20 52.4	$2.49 \pm 0.57$
SMA-4	14 23 48.14	24 04 11.1	$2.70 \pm 0.51$	14 23 48.51	24 04 14.1	$2.64 \pm 0.54$
SMA-5	21 53 34.63	17 40 31.2	$3.39 \pm 0.64$	21 53 34.50	17 40 29.2	$2.49 \pm 0.56$
SMA-6	21 53 38.69	17 42 17.2	$4.01 \pm 0.66$	21 53 38.86	17 42 17.6	$1.97 \pm 0.43$

TABLE 5  
LENS MODELS USED FOR EACH CLUSTER FIELD

Field	Models
A370	Bradac-v1 CATS-v1 Merten-v1 Sharon-v2 Williams-v2 Zitrin-LTM-v1 Zitrin-LTM-Gauss-v1 Zitrin-NFW-v1
MACSJ0717	Bradac-v1 CATS-v4.1 Diego-v4.1 GLAFIC-v3 Keeton-v4 Merten-v1 Sharon-v4 Williams-v4 Zitrin-LTM-v1 Zitrin-LTM-Gauss-v1
A1689	Limousin et al. (2007)
MACSJ1423	Zitrin-LTM-Gauss-v2 Zitrin-NFW-v2
A2390	Richard et al. (2010)

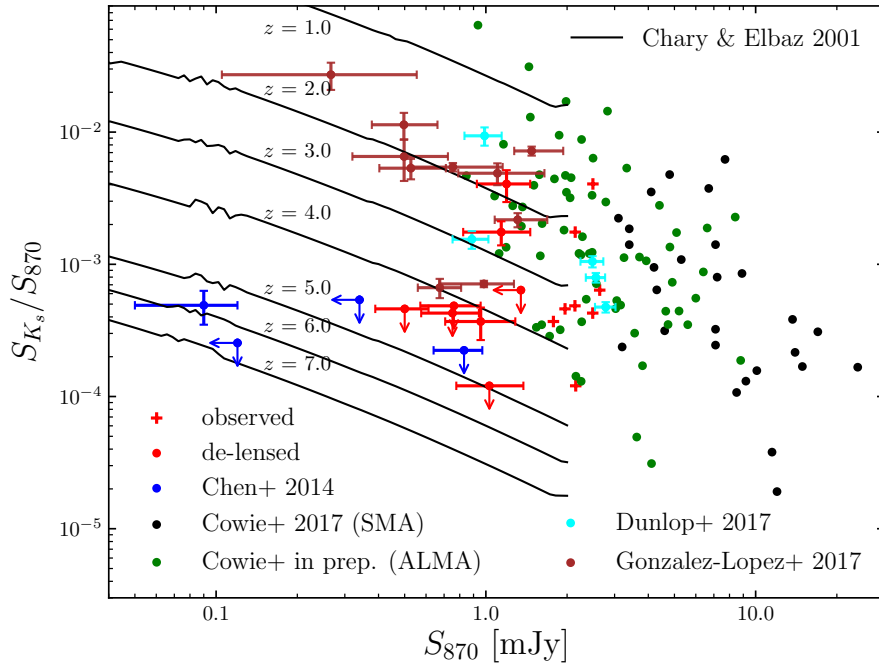


FIG. 2.—  $K_s$ -to-870  $\mu\text{m}$  flux ratios versus 870  $\mu\text{m}$  flux densities of our SMA-detected SMGs (red crosses: observed; red circles: de-lensed) and other samples. Blue circles represent SMA-detected lensed SMGs in A1689 and A2390 from Chen et al. (2014). Cyan circles are ALMA-detected 1.3 mm sources in HUDF from Dunlop et al. (2017), and we scaled their flux densities to 870  $\mu\text{m}$  values assuming an Arp 220 SED (Silva et al. 1998). ALMA-detected lensed SMGs from González-López et al. (2017), and we scaled their flux densities to 870  $\mu\text{m}$  values. The flux densities of Chen et al. (2014) and González-López et al. (2017) are shown in brown, where we again used an Arp 220 SED to scale their 1.1 mm flux densities to 870  $\mu\text{m}$  values. The flux densities of Chen et al. (2014) and González-López et al. (2017) are corrected for lensing magnifications. Black circles are SMA-detected bright SMGs in CDF-N from Cowie et al. (2017). ALMA-detected SMGs in CDF-S (Cowie et al., in preparation) are shown in green. The predictions based on the SED templates of Chary & Elbaz (2001) at various redshifts are plotted in black curves. There is a trend of increasing  $K_s$ -to-870  $\mu\text{m}$  flux ratio with decreasing flux density for most of the sources. However, the majority of SMA-detected lensed SMGs do not follow the same trend.

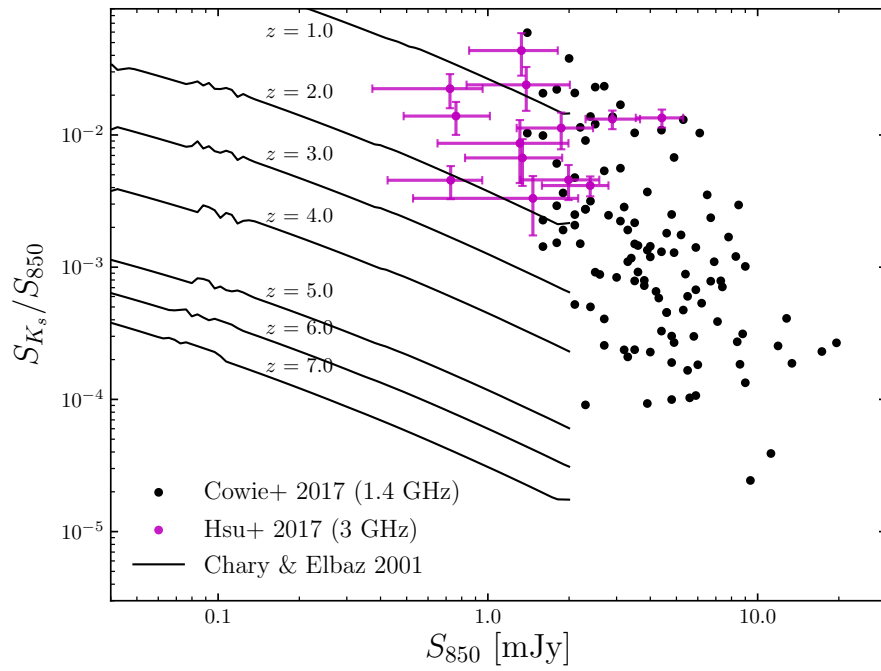


FIG. 3.—  $K_s$ -to-850  $\mu\text{m}$  flux ratios versus SCUBA-2 850  $\mu\text{m}$  flux densities of the bright SMGs identified with VLA 1.4 GHz in CDF-N (black) from Cowie et al. (2017) and the lensed SMGs identified with VLA 3 GHz (purple) from Hsu et al. (2017). Note that one of the 14 sources (0717-2) in Hsu et al. (2017) is removed because it corresponds to SMA-2-1 in this work. The predictions based on the SED templates of Chary & Elbaz (2001) at various redshifts are plotted in black curves.

TABLE 6  
REDSHIFTS, LENSING MAGNIFICATIONS, DE-LENSED SUBMILLIMETER  
FLUX DENSITIES, AND OBSERVED  $K_s$ -BAND MAGNITUDES OF THE  
SMA SOURCES

ID	$z$	$\mu$	$S_{870,\text{int}}$ (mJy)	$m_{K_s}$ (mag)
SMA-1	$2.39 \pm 0.17$	$1.88^{+0.35}_{-0.26}$	$1.14 \pm 0.32$	22.5
SMA-2-1	$2.9 \pm 0.4$	$1.86^{+0.26}_{-0.49}$	$0.96^{+0.33}_{-0.25}$	$24.4 \pm 0.2$
SMA-2-2	$> 3.7$	$2.09^{+0.34}_{-0.59}$	$1.03^{+0.35}_{-0.25}$	$> 25.4$
SMA-3-1	...	$2.81^{+0.10}_{-0.20}$	$0.76^{+0.20}_{-0.19}$	$> 23.8$
SMA-3-2	...	$3.31^{+0.15}_{-0.35}$	$0.75^{+0.19}_{-0.18}$	$> 23.8$
SMA-4	...	$> 1.96$	$< 1.35$	$> 23.3$
SMA-5	$2.00 \pm 0.15$	$2.09 \pm 0.02$	$1.19 \pm 0.27$	$21.4 \pm 0.2$
SMA-6	$> 2.2$	$3.96^{+0.12}_{-0.20}$	$0.50 \pm 0.11$	$> 24.0$

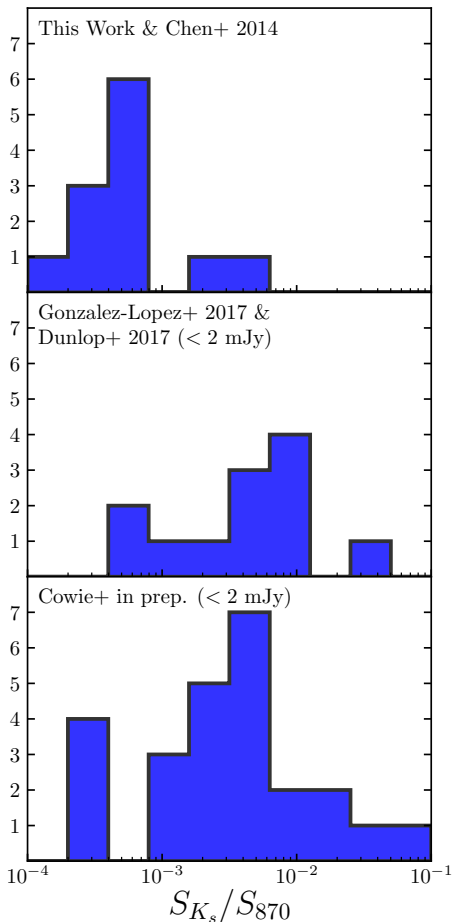


FIG. 4.— Histograms of the  $K_s$ -to-870  $\mu\text{m}$  flux ratios for various samples of faint SMGs. Top: SMA-detected sources from this work and Chen et al. (2014). Middle: González-López et al. (2017) and the sources that are fainter than 2 mJy from Dunlop et al. (2017), with the flux densities scaled to 870  $\mu\text{m}$  values. Bottom: the sources that are fainter than 2 mJy from Cowie et al. (in preparation). The median (de-lensed) 870  $\mu\text{m}$  flux densities for these samples are 0.80, 0.82, and 1.54 mJy, respectively. A K-S test suggests that the top and middle samples are not drawn from the same distribution.

roughly the same space of the diagrams. However, the majority of SMA-detected lensed SMGs from Chen et al. (2014) and this work do not seem to be drawn from the same population to which the other samples belong. In Figure 4, we compare the distributions of the  $K_s$ -to-870  $\mu\text{m}$  flux ratios for

the SMA-detected lensed SMGs from this work and Chen et al. (2014), the ALMA-detected lensed 1.1 mm sources (González-López et al. 2017) and 1.3 mm sources (Dunlop et al. 2017) that are fainter than 2 mJy at 870  $\mu\text{m}$ , and the ALMA-detected blank-field SMGs (Cowie et al., in preparation) that are fainter than 2 mJy. The median (de-lensed) 870  $\mu\text{m}$  flux densities for these three samples are 0.80, 0.82, and 1.54 mJy, respectively. A K-S test for the first and the second samples results in a  $p$ -value  $< 0.001$  and therefore suggests that they are not drawn from the same distribution. Note that SMA-1 and SMA-5, the two sources that have the highest  $K_s$ -to-870  $\mu\text{m}$  flux ratios among our SMA sample (see Figures 2 and 4), are both detected at 1.4 GHz above a  $4\sigma$  level.

We can see a bimodal color distribution in the left side of Figure 2. This suggests that besides optically bright and/or low-redshift sources, there is a population of faint SMGs that are extremely dusty and/or at very high redshifts. However, based on the K-S test, there might be a selection bias in our SMA samples. These sources were chosen for SMA observations because they were candidates to be highly magnified SMGs, especially for the ones of Chen et al. (2014). ALMA imaging of our SCUBA-2 sources in the cluster centers will be the best approach to obtain a large and even sample of faint SMGs. Given the efficiency of ALMA observations, other pre-selections based on magnifications or observed flux densities are not required. As a consequence, we will be able to decide whether the bimodality we observe here really exists.

## 5. SUMMARY

We carried out SMA observations of six intrinsically faint 850  $\mu\text{m}$  sources detected by SCUBA-2 in lensing cluster fields, A1689, A2390, A370, MACSJ0717.5+3745, and MACSJ1423.8+2404, yielding a total of eight SMA detections. Two of the SCUBA-2 sources split into doublets. Based on the lens models from the literature, the intrinsic 870  $\mu\text{m}$  flux densities of these SMGs are  $\sim 1$  mJy. Five of the sources have no optical or NIR counterparts. The NIR-to-submillimeter flux ratios of these faint SMGs suggest that most of them are extremely dusty and/or at very high redshifts. Combining this work and several other samples of SMGs identified with ALMA or SMA, we found a bimodal distribution for the faint sources in the space of submillimeter flux versus NIR-to-submillimeter flux ratio. However, there might be a selection bias in the SMA-detected lensed sources (this work and Chen et al. 2014). Future ALMA observations of a large sample of SCUBA-2 sources in cluster fields will allow us to decide whether the bimodality we observe here really exists.

We gratefully acknowledge support from NSF grants AST-0709356 (L.-Y. H. and L. L. C.) and AST-1313150 (A. J. B.), as well as the John Simon Guggenheim Memorial Foundation and Trustees of the William F. Vilas Estate (A. J. B.). James Clerk Maxwell Telescope is operated by the East Asian Observatory on behalf of The National Astronomical Observatory of Japan, Academia Sinica Institute of Astronomy and Astrophysics, the Korea Astronomy and Space Science Institute, the National Astronomical Observatories of China and the Chinese Academy of Sciences (Grant No. XDB09000000), with additional funding support from the Science and Technology Facilities Council of the United Kingdom and participating universities in the United Kingdom and Canada. The James Clerk Maxwell Telescope has

historically been operated by the Joint Astronomy Centre on behalf of the Science and Technology Facilities Council of the United Kingdom, the National Research Council of Canada and the Netherlands Organisation for Scientific Research. Additional funds for the construction of SCUBA-2 were pro-

vided by the Canada Foundation for Innovation. The National Radio Astronomy Observatory is a facility of the National Science Foundation operated under cooperative agreement by Associated Universities, Inc. We acknowledge the cultural significance that the summit of Mauna Kea has to the indigenous Hawaiian community.

## REFERENCES

- Ammons, S. M., Wong, K. C., Zabludoff, A. I., & Keeton, C. R. 2014, *ApJ*, 781, 2
- Barger, A. J., Cowie, L. L., & Richards, E. A. 2000, *AJ*, 119, 2092
- Barger, A. J., Cowie, L. L., Chen, C.-C., et al. 2014, *ApJ*, 784, 9
- Beckwith, S. V. W., Stiavelli, M., Koekemoer, A. M., et al. 2006, *AJ*, 132, 1729
- Benítez, N. 2000, *ApJ*, 536, 571
- Bertin, E., & Arnouts, S. 1996, *A&AS*, 117, 393
- Bertin, E., Mellier, Y., Radovich, M., et al. 2002, in *Astronomical Society of the Pacific Conference Series*, Vol. 281, *Astronomical Data Analysis Software and Systems XI*, ed. D. A. Bohlender, D. Durand, & T. H. Handley, 228
- Blain, A. W., Smail, I., Ivison, R. J., Kneib, J.-P., & Frayer, D. T. 2002, *Phys. Rep.*, 369, 111
- Bradač, M., Schneider, P., Lombardi, M., & Erben, T. 2005, *A&A*, 437, 39
- Bradač, M., Treu, T., Applegate, D., et al. 2009, *ApJ*, 706, 1201
- Brammer, G. B., Marchesini, D., Labbé, I., et al. 2016, *ApJS*, 226, 6
- Bruzual, G., & Charlot, S. 2003, *MNRAS*, 344, 1000
- Bundy, K., Ellis, R. S., Conselice, C. J., et al. 2006, *ApJ*, 651, 120
- Caminha, G. B., Grillo, C., Rosati, P., et al. 2017, *A&A*, 600, A90
- Casey, C. M., Narayanan, D., & Cooray, A. 2014, *Phys. Rep.*, 541, 45
- Chabrier, G. 2003, *PASP*, 115, 763
- Chary, R., & Elbaz, D. 2001, *ApJ*, 556, 562
- Chen, C.-C., Cowie, L. L., Barger, A. J., et al. 2013, *ApJ*, 776, 131
- Chen, C.-C., Cowie, L. L., Barger, A. J., Wang, W.-H., & Williams, J. P. 2014, *ApJ*, 789, 12
- Coe, D., Bradley, L., & Zitrin, A. 2015, *ApJ*, 800, 84
- Condon, J. J. 1974, *ApJ*, 188, 279
- Cowie, L. L., Barger, A. J., Hsu, L.-Y., et al. 2017, *ApJ*, 837, 139
- Diego, J. M., Protopapas, P., Sandvik, H. B., & Tegmark, M. 2005a, *MNRAS*, 360, 477
- Diego, J. M., Sandvik, H. B., Protopapas, P., et al. 2005b, *MNRAS*, 362, 1247
- Diego, J. M., Tegmark, M., Protopapas, P., & Sandvik, H. B. 2007, *MNRAS*, 375, 958
- Diego, J. M., Broadhurst, T., Benítez, N., et al. 2015, *MNRAS*, 446, 683
- Dole, H., Lagache, G., Puget, J.-L., et al. 2006, *A&A*, 451, 417
- Dunlop, J. S., McLure, R. J., Biggs, A. D., et al. 2017, *MNRAS*, 466, 861
- Dye, S., Eales, S. A., Aretxaga, I., et al. 2008, *MNRAS*, 386, 1107
- Eddington, A. S. 1913, *MNRAS*, 73, 359
- Fixsen, D. J., Dwek, E., Mather, J. C., Bennett, C. L., & Shafer, R. A. 1998, *ApJ*, 508, 123
- Fontana, A., Dunlop, J. S., Paris, D., et al. 2014, *A&A*, 570, A11
- Franceschini, A., Rodighiero, G., Cassata, P., et al. 2006, *A&A*, 453, 397
- González-López, J., Bauer, F. E., Romero-Cañizales, C., et al. 2017, *A&A*, 597, A41
- Grillo, C., Suyu, S. H., Rosati, P., et al. 2015, *ApJ*, 800, 38
- Heavens, A., Panter, B., Jimenez, R., & Dunlop, J. 2004, *Nature*, 428, 625
- Ho, P. T. P., Moran, J. M., & Lo, K. Y. 2004, *ApJL*, 616, L1
- Hoag, A., Huang, K.-H., Treu, T., et al. 2016, *ApJ*, 831, 182
- Holland, W. S., Bintley, D., Chapin, E. L., et al. 2013, *MNRAS*, 430, 2513
- Hsu, L.-Y., Cowie, L. L., Chen, C.-C., Barger, A. J., & Wang, W.-H. 2016, *ApJ*, 829, 25
- Hsu, L.-Y., Desai, V., Murphy, E. J., et al. 2017, *ApJ*, 840, 29
- Jauzac, M., Jullo, E., Kneib, J.-P., et al. 2012, *MNRAS*, 426, 3369
- Jauzac, M., Clément, B., Limousin, M., et al. 2014, *MNRAS*, 443, 1549
- Jauzac, M., Richard, J., Jullo, E., et al. 2015a, *MNRAS*, 452, 1437
- Jauzac, M., Jullo, E., Eckert, D., et al. 2015b, *MNRAS*, 446, 4132
- Johnson, T. L., Sharon, K., Bayliss, M. B., et al. 2014, *ApJ*, 797, 48
- Jullo, E., & Kneib, J.-P. 2009, *MNRAS*, 395, 1319
- Jullo, E., Kneib, J.-P., Limousin, M., et al. 2007, *New Journal of Physics*, 9, 447
- Kawamata, R., Oguri, M., Ishigaki, M., Shimasaku, K., & Ouchi, M. 2016, *ApJ*, 819, 114
- Keeton, C. R. 2010, *General Relativity and Gravitation*, 42, 2151
- Kneib, J.-P., Ellis, R. S., Smail, I., Couch, W. J., & Sharples, R. M. 1996, *ApJ*, 471, 643
- Laporte, N., Bauer, F. E., Troncoso-Iribarren, P., et al. 2017, *ArXiv e-prints*
- Le Floc'h, E., Papovich, C., Dole, H., et al. 2005, *ApJ*, 632, 169
- Liesenborgs, J., De Rijcke, S., & Dejonghe, H. 2006, *MNRAS*, 367, 1209
- Limousin, M., Richard, J., Jullo, E., et al. 2007, *ApJ*, 668, 643
- Lotz, J. M., Koekemoer, A., Coe, D., et al. 2017, *ApJ*, 837, 97
- Madau, P., & Dickinson, M. 2014, *ARA&A*, 52, 415
- Magliocchetti, M., Santini, P., Rodighiero, G., et al. 2011, *MNRAS*, 416, 1105
- McCully, C., Keeton, C. R., Wong, K. C., & Zabludoff, A. I. 2014, *MNRAS*, 443, 3631
- Merten, J., Cacciato, M., Meneghetti, M., Mignone, C., & Bartelmann, M. 2009, *A&A*, 500, 681
- Merten, J., Coe, D., Dupke, R., et al. 2011, *MNRAS*, 417, 333
- Mobasher, B., Dahlen, T., Hopkins, A., et al. 2009, *ApJ*, 690, 1074
- Mohammed, I., Liesenborgs, J., Saha, P., & Williams, L. L. R. 2014, *MNRAS*, 439, 2651
- Oguri, M. 2010, *PASJ*, 62, 1017
- Postman, M., Coe, D., Benítez, N., et al. 2012, *ApJS*, 199, 25
- Puget, J.-L., Abergel, A., Bernard, J.-P., et al. 1996, *A&A*, 308, L5
- Reddy, N. A., Erb, D. K., Pettini, M., Steidel, C. C., & Shapley, A. E. 2010, *ApJ*, 712, 1070
- Richard, J., Smith, G. P., Kneib, J.-P., et al. 2010, *MNRAS*, 404, 325
- Richard, J., Jauzac, M., Limousin, M., et al. 2014, *MNRAS*, 444, 268
- Sault, R. J., Teuben, P. J., & Wright, M. C. H. 1995, in *Astronomical Society of the Pacific Conference Series*, Vol. 77, *Astronomical Data Analysis Software and Systems IV*, ed. R. A. Shaw, H. E. Payne, & J. J. E. Hayes, 433
- Schlafly, E. F., & Finkbeiner, D. P. 2011, *ApJ*, 737, 103
- Sebesta, K., Williams, L. L. R., Mohammed, I., Saha, P., & Liesenborgs, J. 2016, *MNRAS*, 461, 2126
- Silva, L., Granato, G. L., Bressan, A., & Danese, L. 1998, *ApJ*, 509, 103
- Wang, W.-H., Cowie, L. L., Barger, A. J., Keenan, R. C., & Ting, H.-C. 2010, *ApJS*, 187, 251
- Wold, I. G. B., Owen, F. N., Wang, W.-H., Barger, A. J., & Keenan, R. C. 2012, *ApJS*, 202, 2
- Zavala, J. A., Aretxaga, I., Geach, J. E., et al. 2017, *MNRAS*, 464, 3369
- Zitrin, A., Broadhurst, T., Umetsu, K., et al. 2009, *MNRAS*, 396, 1985
- Zitrin, A., Meneghetti, M., Umetsu, K., et al. 2013, *ApJL*, 762, L30